High-throughput Computational Design of Organic-inorganic Hybrid Halide Semiconductors Beyond Perovskites for Optoelectronics

Journal:	*Energy & Environmental Science*
Manuscript ID	EE-ART-04-2019-001371.R1
Article Type:	Paper
Date Submitted by the Author:	15-May-2019
Complete List of Authors:	Li, Yuheng; University of California San Diego, NanoEngineering Yang, Kesong; University of California San Diego, NanoEngineering

Journal Name

ARTICLE TYPE

Cite this: DOI: 10.1039/xxxxxxxxxx

High-throughput Computational Design of Organic-inorganic Hybrid Halide Semiconductors beyond Perovskites for Optoelectronics†

Yuheng Li[a] and Kesong Yang[a,b,c]

Received Date
Accepted Date

DOI: 10.1039/xxxxxxxxxx

www.rsc.org/journalname

Organic-inorganic lead halide perovskites show great promise in optoelectronic applications such as light-emitting diodes and solar energy conversion. However, the poor stability and toxicity of lead halide perovskites severely limit their large-scale applications. Here we show a high-throughput design of lead-free hybrid halide semiconductors with robust materials stability and desired material properties beyond perovskites. On the basis of 24 prototype structures that include perovskite and non-perovskite structures and several typical organic cations, a comprehensive quantum materials repository that contains 4507 hypothetical hybrid compounds was built using large-scale first-principles calculations. After a high-throughput screening of this repository, we have rapidly identified 23 candidates for light-emitting diodes and 13 candidates for solar energy conversion. Our work demonstrates a new avenue to design novel organic-inorganic functional materials by exploring a great variety of prototype structures.

1 Introduction

Organic-inorganic hybrid lead halide perovskites with a prototypical formula of $MAPbI_3$ ($MA=CH_3NH_3$) are one emerging class of semiconductor materials with promising optoelectronic applications including solar energy conversion and light-emitting diodes.[1,2] This is mainly attributed to their excellent materials properties such as tunable band gaps[3], high charge carrier mobility[4], defect tolerance[5], and low-temperature solution processability[6]. In spite of their promising optoelectronic applications, particularly for solar energy conversion, the hybrid lead halide perovskites are facing two major challenges including poor stability and presence of toxic lead, which limits their large-scale applications.[7,8] To overcome these challenges, one solution is to search for novel hybrid materials with potentially superior properties beyond or like that of lead-based hybrid halide perovskites.

Some prior experimental and computational efforts both have been made to explore alternatives to lead halide perovskites. There are two major classes of candidates that are being extensively studied. One class of candidates are Ge- and Sn-based halide perovskites with various organic cations, but these materials usually have even lower stability than lead halide perovskites.[9] To enhance stability of Sn-based perovskites, some experimental approaches such as the fabrication of low-dimensional structures[10] and the encapsulation of device[11] have been proposed. In addition to Ge and Sn, Si mixed with other cations such as Ca/Si and Zn/Si with different ratios were also tried.[12] The other class of candidates are called double perovskites with a chemical formula $A_2BB'X_6$ (A=Cs or organic cations; X=Cl, Br, or I), which can be regarded as derivatives of single perovskite $MAPbX_3$ but with Pb replaced by two different metal cations ($B=B^+$; $B'=B^{3+}$).[13–19] Early experimental demonstration of double perovskites for optoelectronics include Cs-based inorganic double perovskites with Ag-Bi composition[13–15] and the MA-based hybrid double perovskite with K-Bi composition.[16] Nevertheless, most double perovskites that are predicted to have good electronic properties often suffer from instability issues such as phase separation or redox decomposition, *e.g.*, $Cs_2InBiCl_6$ and $Cs_2InSbCl_6$,[20] while double perovskites that can be synthesized usually show large indirect band gaps.[13–16] Despite this, extensive research efforts are being made to search for novel double perovskites with desired electronic properties and high stability, such as using high-throughput materials design approach,[17–19] towards lead-free perovskite optoelectronics.[21–23]

Notably, these prior efforts primarily focused on the single perovskite structure with a stoichiometry of 1:1:3 or on the double perovskite with a stoichiometry of 2:1:1:6. Besides perovskite structures, there exist in principles other organic-inorganic hybrid ternary metal halide compounds with appropriate metal elements and the stoichiometry of component elements that are more sta-

---

[a] *Department of NanoEngineering, University of California San Diego, 9500 Gilman Drive, Mail Code 0448, La Jolla, California 92093-0448, USA.* [b] *Program of Materials Science and Engineering, University of California San Diego, La Jolla, California 92093-0418, USA.* [c] *Center for Memory and Recording Research, University of California San Diego, La Jolla, California 92093-0401, USA.* Fax: +1-858-534-9553; Tel: +1-858-534-2514; E-mail: kesong@ucsd.edu

ble and even show better optoelectronic properties than the typical perovskite structures.[24] As a proof of concept, Sb-based hybrid ternary compound, $(MA)_3Sb_2Cl_xI_{9-x}$, has been prepared, and the solar cell based on this material reached a power conversion efficiency over 2%;[25] the ternary silver bismuth iodides showed tunable optoelectronic properties upon sulfide modification for photovoltaics.[26] Therefore, it is worthwhile to explore non-perovskite ternary structures for searching for alternatives to lead halide perovskites.

In this work, we have carried out a high-throughput computational design of novel lead-free organic-inorganic ternary halide semiconductors for optoelectronic applications using large-scale first-principles electronic structure calculations and have successfully identified 13 candidates for photovoltaic applications and 23 candidates for light-emitting applications. The chemical formulas of selected candidates include A_2BX_4, $A_3B_2X_9$, and A_2BX_6, in which A = MA, FA, or AD, and X=Cl, Br, or I. All these candidates have robust materials stability, appropriate band gaps, effective masses, and exciton binding energies for the optoelectronic applications.

2 Methods

The high-throughput first-principles calculations were performed using the automatic framework AFLOW[27] based on the Vienna *Ab-initio* Simulation Package (VASP).[28] The projector augmented wave potentials, and the generalized gradient approximation (GGA) of the exchange-correlation functional as parameterized by Perdew, Burek, and Ernzerhof (PBE) are used in the DFT calculations.[29] To properly describe the long-range dispersion interactions between the organic molecules in the hybrid materials, two types of van der Waals (vdW) functionals including DFT-D3[30] and optB86b[31] were carefully assessed for the prototype compound $MASnBr_3$, along with the standard PBE functional. As shown in Table S1 of Supporting Information, our test calculations suggest that both vdW functionals give more accurate equilibrium lattice parameters than the PBE functional while the DFT-D3 method shows a better match with the experimental value than the optB86b and thus is used in our calculations. Structures are fully relaxed with a convergence tolerance of 0.01 meV/atom. k-points grid of 0.05 $Å^{-1}$ were automatically set for relaxation of different structures. Accurate charge densities and density of states are obtained in static calculations with a denser grid of 0.04 $Å^{-1}$. Other computational settings such as cutoff energy are managed by the AFLOW code that also generates appropriate entries for the structural relaxation, static calculations, and the electronic band structure calculations sequentially and automatically.[27] The hybrid DFT calculations within Heyd-Scuseria-Ernzerhof (HSE) formalism with 25% Hartree-Fock (HF) exchange are employed to predict accurate band gaps for the candidate compounds.[32,33] The parameter of 25% HF mixing constant was derived from perturbation theory,[32,33] which can generally yield close band gaps to the experiment and is appropriate for a large number and variety of hypothetical compounds.[17,18]

Table 1 Structural properties of the $Cs_xB_yX_z$ compounds used to extract prototype structures. Original inorganic compound, space group, ICSD number, and Pearson symbol. All the prototype structures are available in the AFLOWLIB and/or Materials Project.

B^{+n}	Stoichiometry	Original Compound	Space Group	ICSD Number	Pearson Symbol
B^{+1}	1:1:2	$Cs_4Ag_4Br_8$	Cmcm	150301	oS16
		$Cs_2Ag_2Cl_4$	P4/nmm	150300	tP8
	1:2:3	$Cs_4Cu_8Br_{12}$	Cmcm	49613	oS24
B^{+2}	1:1:3	$Cs_1Sn_1Br_3$	$Pm\bar{3}m$	4071	cP5
		$Cs_1Ge_1Br_3$	R3m	80317	hR5
		$Cs_3Mn_3Cl_9$	$R\bar{3}m$	2555	hR15
		$Cs_4Ag_4Cl_{12}$	I4/mmm	66067	tI20
		$Cs_2Cd_2Br_6$	$P6_3mc$	281176	hP10
		$Cs_2Dy_2Br_6$	P4/mbm	300285	tP10
		$Cs_4Cr_4I_{12}$	Pbcn	23383	oP20
		$Cs_4Sn_4I_{12}$	$P2_1/m$	14070	mP20
		$Cs_4Cr_4Cl_{12}$	C2/m	41802	mS20
		$Cs_4Pb_4I_{12}$	Pnma	161480	oP20'
	2:1:4	$Cs_4Cd_2Cl_8$	I4/mmm	16576	tI14
		$Cs_8Pd_4Cl_{16}$	Cmmm	95812	oS28
		$Cs_4Hg_2I_8$	$P2_1/m$	63110	mP14
		$Cs_8Zn_4Br_{16}$	Pnma	69139	oP28
	2:3:8	$Cs_4Hg_6I_{16}$	Cm	4074	mS26
	1:2:5	$Cs_2Hg_4Br_{10}$	$P2_1/m$	200751	mP16
B^{+3}	3:2:9	$Cs_3Bi_2Br_9$	$P\bar{3}m1$	1142	hP14
		$Cs_6Mo_4Br_{18}$	$P6_3/mmc$	26213	hP28
B^{+4}	2:1:6	$Cs_4Pd_2I_{12}$	I4/mmm	280189	tI18
		$Cs_8Pt_4Br_{24}$	$Fm\bar{3}m$	77381	cF36
		Cs_2CeCl_6	$P\bar{3}m1$	14339	hP9

3 Results

3.1 Building Repository

As the first step, we built a quantum materials repository that contains hybrid halide perovskites and perovskite derivatives. To do this, we began by identifying all possible prototype structures based on existing ternary metal halide compounds with a formula of $Cs_xB_yX_z$ from the online quantum materials databases AFLOWLIB[34] and Materials Project.[35] The reason for selecting Cs-contained compounds is as follows. The Cs cation has a large ionic radius that is comparable with that of the organic cations such as MA, and thus it can be readily substituted by organic cations to form organic-inorganic hybrid compounds. Note that one chemical formula may correspond to different crystal structures, and only the most stable one was selected as a prototype structure. As shown in Fig. S1 of the Supporting Information, a total number of 24 unique prototype structures were identified. Their complete structural information is listed in Table 1, including space group, ICSD number, and Pearson symbol. The unique Pearson symbol is used to denote these prototype structures. For example, the structure generated from the compound $CsSnBr_3$ with a space group of $Pm\bar{3}m$ and an ICSD number of 4071 (identifed as CsSnBr3_ICSD_4071 in AFLOWLIB) is denoted using its Pearson symbol of cP5. The prototype structures cP5 and tI20 (tP10) are the cubic and tetragonal perovskites, respectively, and

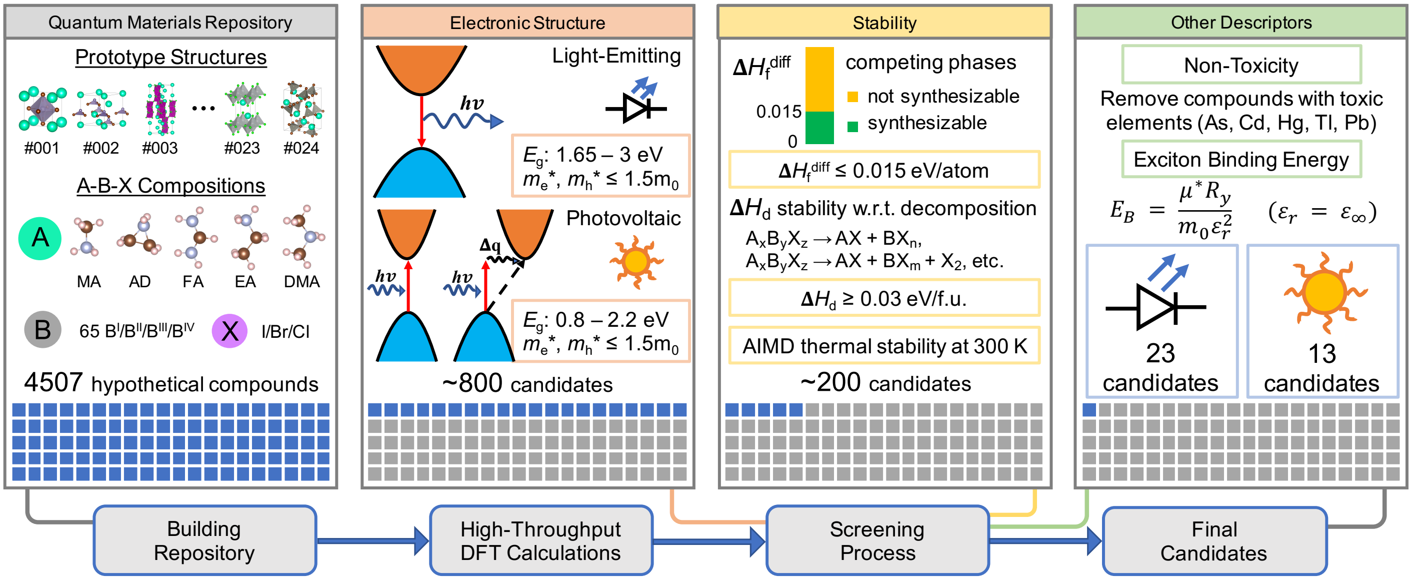

Fig. 1 Schematic diagram of the high-throughput screening process. A total number of 4507 compounds ($A_xB_yX_z$, A = MA/FA/AD/EA/DMA, X = I/Br/Cl) were generated from 65 kinds of B-site elements in 24 different crystal structures. Compounds with direct band gaps in the visible spectrum range are kept for light-emitting materials, and compounds with band gaps in 0.8-2.2 eV are kept for solar-cell materials. Compounds with effective masses greater than 1.5m$_0$ are excluded. Compounds with a formation enthalpy higher than its most energetically favorable competing phase by a value greater than 0.015 eV/atom are excluded. Compounds containing toxic B-site elements are also excluded. Compounds that cannot maintain structural integrity at room temperature are excluded. The selected candidates are all stable with respect to decomposition by at least 0.03 eV/formula unit. Compounds with exciton binding energy greater than 130 meV are excluded for solar-cell materials. 23 candidates for light-emitting materials and 13 candidates for solar-cell materials were selected.

the others are perovskite derivatives. Note that two prototypes, CsCrI$_3$_ICSD_23383 and CsPbI$_3$_ICSD_161480, share the same Pearson symbol of oP20, and to distinguish them, we denote the former with oP20, and the later with oP20'.

After identifying the structure prototypes, we next generate hypothetical compounds by placing various elements in the $A_xB_yX_z$ formula. At A site, we put relatively small organic cations, including MA (CH_3NH_3), FA ($CH(NH_2)_2$), AD ($(CH_2)_2NH_2$)[36], DMA ($NH_2(CH_3)_2$), and EA ($C_2H_5NH_3$). At B site, we select elements with different valence states according to the different stoichiometry of $A_xB_yX_z$. As shown in Table 1, there are three structure prototypes for B^+, 16 prototypes for B^{2+}, two prototypes for B^{3+}, and three prototypes for B^{4+}. B^+-based prototypes have two different stoichiometries (A:B:X=1:1:2 and 1:2:3); B^{2+}-based prototypes have four different stoichiometries (A:B:X=1:1:3, 2:1:4, 2:3:8, and 1:2:5); B^{3+}-based prototypes only have one stoichiometry (A:B:X=3:2:9); and B^{4+}-based prototypes also only have one stoichiometry (A:B:X=2:1:6). A total number of 65 possible B-site elements with common valence states from +1 to +4 were placed in the corresponding prototypes. The X site is occupied by I, Br, or Cl ions. With the three sites combined in the 24 prototypes, a total number of 4507 hypothetical compounds were generated. The electronic structure of all the compounds is computed in a high-throughput fashion.

3.2 Screening Process

In terms of optoelectronic applications like solar cells and light emitters, there are several common descriptors often used for high-throughput screening of target materials. These descriptors include band gap, charge carrier effective masses, and decomposition enthalpy. Our detailed criteria for each descriptor are discussed as below:

(i) Band gap (E_g). We obtained band gaps using DFT calculations with two different types of functionals: One is calculated with the standard GGA functional (E_g^{GGA}), and the other is calculated with the hybrid functionals (E_g^{HSE})[32]. This is because the GGA functional often underestimate band gaps, thus E_g^{GGA} can only serve as a rough reference for screening; while E_g^{HSE} is much closer to the experimental value, as shown from previous calculations on halide perovskites,[17,18,37] and thus it can be used to select promising compounds more accurately. For compounds that contain heavy elements with atomic number ≥ 72, we also incorporated spin-orbit coupling (SOC) to get more accurate E_g.[38] Note that requirements for E_g are different in solar-cell and light-emitter applications. For solar cells, the light-absorbing materials can have either direct or indirect band gaps. The optimal band gap energy should be in the range from 0.8 to 2.2 eV. This range is selected according to the relationship between Shockley-Queisser efficiency limit and band gap energy.[39] For light emitters, the energy of photons emitted by a light-emitting material is approximately equal to the band gap energy of the material ($E_{photon} = E_g + k_BT/2$, k_BT is thermal energy). Therefore, for visible-light emission excluding short-wavelength violet light, we selected materials with E_g^{HSE} in the range from 1.65 to 3.0 eV. Note that this range partially overlap with the range required for solar cell materials. The overlap demands discrimination in exciton binding energy of the materials with E_g in 1.65 - 2.2 eV to decide their proper applications, which will be discussed in (vii). In terms of band gap type, direct band gaps are required for a high photon-emission efficiency.[2] This is because a direct band gap greatly promotes radiative recombination of electron-hole pairs, which results in more photons emitted. In contrast, for an indirect-band gap material, radiative recombination is much less likely because phonons are required in the process.[40,41] Therefore, indirect transition is detrimental to light-emitting materials. As the opposite process to the carrier-recombination and photon-emission in light-emitting materials, the light-absorption and electron-excitation process in solar-cell materials is also adversely affected by indirect transition with the same mechanism. However, the poor absorption and excitation can be compensated by increasing the thickness of absorbing layer made of indirect-band gap material, as long as the material has a long minority carrier diffusion length to guarantee carrier separation and collection across the solar cell device.[41–43] For example, silicon (indirect band gap) absorbers are made much thicker than GaAs (direct band gap) absorbers to absorb more light, and long minority diffusion length of Si ensures photogenerated carriers to cross the device before recombination.

(ii) Electron and hole effective masses (m_e^* and m_h^*). Small and balanced carrier effective masses are required for both solar cells and light emitters. This is because the photovoltaic and electroluminescence processes both require efficient carrier transport, which is beneficial for charge separation in solar cells and charge recombination in light emitters.[44] m_e^* and m_h^* are calculated by fitting band structures near the band edges according to the equations: $\frac{1}{m_e^*} = \frac{1}{\hbar^2}\frac{\partial^2 E_C}{\partial k^2}$, and $\frac{1}{m_h^*} = \frac{1}{\hbar^2}\frac{\partial^2 E_V}{\partial k^2}$. That is, m_e^* is derived from the curvature of the bottom conduction bands near the conduction band minimum (CBM) and m_h^* is derived from the curvature of the top valence bands near the valence band maximum (VBM). Note that the CBM (VBM) involves two reciprocal paths in the high-throughput electronic structure calculations, and only the smaller value of m_e^* (m_h^*) is used as the materials descriptor for the anisotropic materials. This is because the such values can best represent the charge transport potential that can be utilized in experiments.[10] Meanwhile, to provide more detailed information on the effective masses near the band edges, we also listed effective masses along the major directions for the anisotropic candidates in Table S2 of the Supporting Information. In addition, to obtain more accurate m_e^* and m_h^* for compounds containing heavy elements (atomic number ≥ 72), the spin-orbit-coupling was included in our electronic structure calculations. In this work, a common upper limit of $1.5m_0$ was used as the screening criterion ($m_e^* \leq 1.5m_0$, $m_h^* \leq 1.5m_0$).[19]

(iii) Formation enthalpy difference (ΔH_f^{diff}). As shown in Table 1, one stoichiometry may correspond to several different prototype structures. This means that there might exist several competing phases for the same composition in the same stoichiometry. For example, the well-known $MAPbI_3$ corresponds to 10 hypothetical compounds as competing phases of each other. To select compounds that can be synthesized in experiments, we define ΔH_f^{diff} as the calculated formation enthalpy difference between each compound and its most energetically favorable competing phase of the same composition and stoichiometry. This is because different stoichiometries can usually be achieved by using precursors of different molar ratios when synthesizing compounds .[45–48] For example, both $MACdBr_3$ and MA_2CdBr_4 have been synthesized via an appropriate control of stoichiometry.[49] All compounds with $\Delta H_f^{diff} \leq 0.015$ eV/atom were selected as synthesizable compounds. This criterion comes from the $MAPbI_3$ example. For $MAPbI_3$, the tetragonal perovskite (tI20) phase is often synthesized in experiments[1,50], while our calculations show that oP20' is the structure with the lowest energy instead of tI20. tI20 for $MAPbI_3$ has a ΔH_f higher than the most stable oP20' by $\Delta H_f^{diff} = 0.015$ eV/atom. This indicates that compounds with such a small ΔH_f^{diff} can be experimentally synthesized.

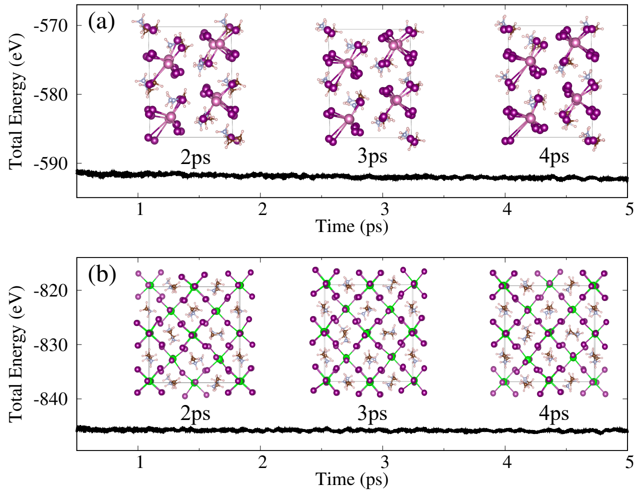

Fig. 2 Total energy during 5ps *ab-initio* molecular dynamics (AIMD) simulations at 300K for two representative hybrid materials: (a) $(MA)_3In_2I_9$ (hP14) and (b) $(MA)_2ZrI_6$ (tI18).

(iv) Decomposition enthalpy (ΔH_d). To ensure stability of selected compounds with respect to decomposition, ΔH_d should be positive for all possible decomposition pathways. In this work, we calculated phase separation of compounds into binary products ($A_xB_yX_z \rightarrow AX + BX_n$), as well as redox decomposition pathways. The pathway with the lowest ΔH_d for each compound is used to determine its stability. We set the criterion as $\Delta H_d > 0.03$ eV/f.u. to ensure relatively high stability of selected compounds.

(v) Compounds with toxic B-site elements (As, Cd, Hg, Tl, Pb) were removed. In addition, because the compositions of our selected perovskite compounds (B = Ge/Sn/Au/Ag/Cu) have all been discovered in prior studies, we excluded all perovskites in the final list.

(vi) Structural integrity at room temperature. To evaluate room-temperature structural stability of candidate materials, *ab-initio* molecular dynamics (AIMD) calculations were carried out at 300K within the van der Waals correction using DFT-D3 method.[30] The entire molecular dynamics simulation lasted 5 ps with a time step of 1 fs using the Nosé-Hoover method. The supercells of 2×2×1 unit cell for the tI14, tI18, hP14, and hP28 structures and the conventional unit cell for cF36 structure were used. As shown in Figure 2 for two representative compounds $(MA)_3In_2I_9$ and $(MA)_2ZrI_6$, the calculated total energies as a func-

Table 2 Properties of selected hybrid halide compounds for light-emitting materials: compound, Pearson symbol of the prototype structures, equilibrium lattice parameters (in Å), calculated band gaps (in eV) from GGA-PBE (E_g^{GGA}) and HSE (E_g^{HSE}) approaches, band gap type and k-point position from VBM to CBM, electron (hole) effective masses m_{e^*} (m_{h^*}) near the CBM (VBM), reduced effective mass (μ), average of exciton binding energies on xx, yy, and zz directions (E_B), and decomposition enthalpy (ΔH_d, in eV/f.u.). In this and next Table, † denotes the calculations with spin orbit coupling; ‡ denotes compounds that are suitable for both light-emitting and solar-cell materials; and $*$ indicates experimental validation of the hybrid compound or its inorganic analogue for optoelectronics.

Compound	Pearson Symbol	Lattice Parameters			E_g^{GGA}	E_g^{HSE}	E_g Type	$k_{VBM} \rightarrow k_{CBM}$	m_e^*	m_h^*	μ	E_B	ΔH_d
		a	b	c									
$(MA)_2GeBr_4$	tI14	5.54	5.54	19.02	1.40	1.99	D	S - S	0.06	0.12	0.04	31.47	0.33
‡$(MA)_2GeI_4$	tI14	5.94	5.87	20.11	1.21	1.66	D	S - S	0.11	0.11	0.06	35.22	0.24
$(MA)_2SnCl_4$	tI14	5.56	5.48	18.35	1.80	2.49	D	S - S	0.55	0.19	0.14	157.62	0.25
‡$(MA)_2SnBr_4$	tI14	5.72	5.74	19.08	1.11	1.67	D	S - S	0.11	0.10	0.05	37.33	0.23
$(MA)_3In_2I_9$	hP14	8.23	8.31	11.00	1.34	2.18	D	Γ - Γ	0.40	0.61	0.24	200.96	0.93
$(MA)_3Sb_2Br_9$	hP14	7.71	7.71	10.37	2.07	2.70	D	Γ - Γ	0.33	0.41	0.18	126.79	1.04
‡$(MA)_3Sb_2I_9$$*$[51]	hP14	8.26	8.26	10.91	1.52	2.02	D	Γ - Γ	0.21	0.31	0.13	53.67	0.75
$(MA)_2ZrI_6$	tI18	8.18	8.19	12.37	1.68	2.60	D	Γ - Γ	0.74	0.98	0.42	306.27	0.77
‡$(FA)_2SnBr_4$	tI14	5.64	5.71	20.60	1.15	1.69	D	S - S	0.61	0.09	0.08	57.66	0.03
$(FA)_3Ga_2I_9$	hP14	7.94	8.25	11.83	1.27	2.17	D	A - A	0.61	1.17	0.40	374.59	0.90
$(FA)_3In_2Br_9$	hP14	7.38	7.83	11.17	1.79	2.91	D	Γ - Γ	0.52	0.60	0.28	351.69	0.69
$(FA)_3In_2I_9$	hP14	8.04	8.30	11.67	1.06	1.90	D	Γ - Γ	0.40	0.38	0.19	156.31	0.71
‡$(FA)_3Bi_2I_9$$*$[52]	hP14	8.06	8.36	11.60	1.79	1.80†	D	Γ - Γ	0.28†	0.58†	0.19†	96.88	0.56
$(FA)_3Sb_2I_9$$*$[53]	hP28	8.02	8.32	23.18	1.97	2.54	D	M - M	0.39	0.68	0.25	155.23	0.79
$(AD)_2GeI_4$	tI14	6.14	6.16	18.97	1.74	2.30	D	S - S	0.14	0.45	0.11	71.77	0.12
$(AD)_2SnBr_4$	tI14	5.87	5.86	18.09	1.78	2.51	D	S - S	0.43	0.34	0.19	150.24	0.22
‡$(AD)_2SnI_4$	tI14	6.22	6.21	19.17	1.33	1.87	D	S - S	0.15	0.25	0.09	48.21	0.30
$(AD)_3Sb_2Br_9$	hP14	8.30	8.36	9.55	1.90	2.52	D	Γ - Γ	0.39	0.43	0.20	151.96	1.43
‡$(AD)_3Sb_2I_9$	hP14	8.69	8.77	10.20	1.43	1.91	D	Γ - Γ	0.26	0.31	0.14	61.17	1.06
$(AD)_3In_2I_9$	hP28	8.61	8.71	20.54	1.13	2.00	D	Γ - Γ	0.50	1.11	0.34	270.00	0.94
$(AD)_2HfI_6$	tI18	8.47	8.46	12.17	2.07	2.89†	D	Γ - Γ	1.28†	0.80†	0.49†	431.53	0.93
$(AD)_2SnBr_6$	tI18	8.13	8.12	11.56	1.36	2.42	D	Γ - Γ	0.51	1.24	0.36	483.68	0.90
$(AD)_2TeBr_6$	tI18	8.29	8.30	11.18	2.14	2.71	D	Γ - Γ	1.14	0.97	0.52	533.26	0.99

tion of time during the 5ps simulation time are oscillating within a rather narrow energy range and the selected geometrical structures at 2, 3, and 4ps all exhibit an ordered crystalline phase, indicating their structural integrity at room temperature.[55] Otherwise, the candidate materials are not stable at room temperature and will be excluded from the final list. The calculated time-dependent total energies for all the final candidate materials are shown in the Supplementary Fig. S2-S6.

(vii) Exciton binding energy (E_B). E_B is the energy required to separate electron-hole pairs (excitons) into free carriers. It is critical to the electron-hole separation and recombination processes in solar cells and light emitters, respectively. A small E_B is beneficial for separation of photogenerated electron-hole pairs in solar cells, but detrimental to charge recombination in light emitters; while a large E_B inhibits separation but promotes recombination. Therefore, E_B discriminates photovoltaic and electroluminescence applications for our final candidates. In this study, we use the hydrogen-like Wannier-Mott model to calculate E_B as an effective Rydberg:[9]

$$E_B = \frac{\mu^* R_y}{m_0 \varepsilon_r^2} \tag{1}$$

It is dependent on effective mass ($\frac{\mu^*}{m_0}$) and screening effect on Coulomb interaction between electrons and holes (represented by relative dielectric constant, ε_r). The high-frequency limit of dielectric constant (ε_∞), which is solely contributed by electronic polarization, is adopted as ε_r, and it is obtained by finite-electric field and Berry-phase calculations. The calculated exciton binding energy of some compounds are anisotropic depending on their crystal structures. We take averaged value of exciton binding energies along three directions as the descriptor ($E_B = \frac{1}{3}(E_B^{xx} + E_B^{yy} + E_B^{zz})$). Our calculations for tetragonal $MAPbI_3$ (tI20) with spin-orbit-coupling interactions yield an E_B about 72 meV, which is comparable to the experimental value (50 meV).[56] In this work, we set the criterion at $E_B \leq 130$ meV for solar-cell materials to include more promising candidates. Such relatively small E_B values are comparable to thermal energy ($k_B T$) at solar-cell operating temperatures and are beneficial for easy dissociation of photogenerated electron-hole pairs before they recombine. For light-emitting materials, we use intrinsic E_B of our candidates as a reference instead of a selection criterion. This is because light-emitting materials like perovskites are usually prepared in nanocrystals to enlarge E_B,[2] and materials with intrinsic small E_B can also be utilized in actual applications.

The above screening process is summarized in Figure 1. The screening gives us 23 final candidates for light emitters (Table 2)

Table 3 Properties of selected hybrid halide compounds for solar-cell materials.

Compound	Pearson Symbol	Lattice Parameters			E_g^{GGA}	E_g^{HSE}	E_g Type	$k_{VBM} \rightarrow k_{CBM}$	m_e^*	m_h^*	μ	E_B	ΔH_d
		a	b	c									
‡$(MA)_2GeI_4$	tI14	5.94	5.87	20.11	1.21	1.66	D	S - S	0.11	0.11	0.06	35.22	0.24
‡$(MA)_2SnBr_4$	tI14	5.72	5.74	19.08	1.11	1.67	D	S - S	0.11	0.10	0.05	37.33	0.23
$(MA)_2SnI_4$	tI14	6.12	6.11	20.00	0.97	1.42	D	S - S	0.18	0.10	0.06	33.81	0.30
‡$(MA)_3Sb_2I_9$*[51]	hP14	8.26	8.26	10.91	1.52	2.02	D	Γ - Γ	0.21	0.31	0.13	53.67	0.75
$(MA)_3Bi_2I_9$	hP14	8.35	8.35	11.00	1.85	1.82†	I	A - Γ	0.41†	0.62†	0.25†	124.88	0.59
$(MA)_2SnI_6$*[54]	cF36	11.61	11.44	12.55	0.09	0.80	D	Γ - Γ	0.22	1.16	0.18	94.82	0.43
$(MA)_2TeI_6$*[54]	cF36	11.67	11.51	12.58	1.27	1.77	I	Γ - L	0.25	1.24	0.21	104.21	0.78
‡$(FA)_2SnBr_4$	tI14	5.64	5.71	20.60	1.15	1.69	D	S - S	0.61	0.09	0.08	57.66	0.03
‡$(FA)_3Bi_2I_9$*[52]	hP14	8.06	8.36	11.60	1.79	1.80†	D	Γ - Γ	0.28†	0.58†	0.19†	96.88	0.56
‡$(AD)_2SnI_4$	tI14	6.22	6.21	19.17	1.33	1.87	D	S - S	0.15	0.25	0.09	48.21	0.30
‡$(AD)_3Sb_2I_9$	hP14	8.69	8.77	10.20	1.43	1.91	D	Γ - Γ	0.26	0.31	0.14	61.17	1.06
$(AD)_3Bi_2I_9$	hP14	8.78	8.84	10.26	1.79	1.80†	I	M - Γ	0.38†	0.48†	0.21†	109.24	0.94
$(AD)_2TeI_6$	cF36	12.54	11.63	12.17	1.24	1.87	I	Γ - L	0.27	1.09	0.22	120.85	0.93

and 13 final candidates for solar cells (Table 3). Among these final candidates, 7 compounds are suitable for both applications.

Besides the seven materials descriptors discussed above, some other materials parameters such as defect tolerance and light absorption are also closely related to the optoelectronic properties. An ideal defect tolerance should have following property: intrinsic defects with low formation energies do not induce deep gap states, while those creating deep gap states have high formation energies.[9,57–59] Such defect tolerance prevents the undesired recombination of photoexcited electrons and holes. A complete defect property study requires considerations of all the possible defects, such as various types of anionic and cationic vacancies, anti-sites defects, and interstitial defects, and even charged defects, in each candidate, which is beyond the scope of this high-throughput screening study. Moreover, our screening process already limits the final candidates to a very small and specific structural and compositional space out of the comprehensive materials repository of over 4500 compounds, and some predicted materials (including their inorganic analogues) have been demonstrated in recent experiments for optoelectronic applications (see Table 2 and 3), indicating a robust credibility of our high-throughput screening approach. As for the light absorption property, as discussed in previous studies, it is largely dependent on the bonding characteristic, band-gap type and values, and band dispersion,[17,60] which have been partially addressed in the screening process and will be discussed later with the electronic structures for the final candidates.

4 Discussion

4.1 Composition and Structure

In this section, we discuss crystal structure and composition of the selected compounds. Table 2 and Table 3 show all the final candidates for light-emitting and photovoltaic materials, respectively. The final candidates based on different organic A cations take the same structures and contain similar B and X elements. Note that EA- and DMA-based compounds are not included in the final lists, because they show relatively low decomposition enthalpy compared to their MA/FA/AD analogues according to our calculations. All the final candidates adopt five out of the 23 prototype structures, with their Pearson numbers being tI14, hP14, hP28, tI18, and cF36, see their structural illustrations in Figure 3a-d and Figure S1 of Supporting Information. The B sites in the five structures correspond to ions of different valence states from +2 to +4, and they greatly determine the compositions of the final candidates. Below we discuss the selected compounds in the order of their B-site valence states.

The B^{2+} candidates all take the tI14 structure (Figure 3a) with a chemical formula of A_2BX_4. tI14 consists of corner-sharing octahedra in a two-dimensional (2D) arrangement. B-site elements of selected tI14 compounds include Ge and Sn. Note that Sn^{2+} or Ge^{2+} oxidation states are metastable and are prone to be oxidized to +4, which could raise concerns about their oxidation stability. However, recent experimental[10] and computational[37] studies both indicate that the 2D hybrid perovskites based on Sn^{2+} or Ge^{2+} show enhanced materials stability compared to the 3D perovskites because of their low-dimensional structural feature, and the low-dimensional structure effectively prevents the oxidation of Sn^{2+} during the film fabrication.[10] Interestingly, unlike traditional perovskites, crystal structure of screened tI14 compounds resemble that of the 2D hybrid perovskites, implying a robust stability of these candidate materials. Moreover, even for traditional perovskites containing Sn^{2+} or Ge^{2+}, some experimental techniques are actively proposed to improve their stability and to prevent the oxidation, such as using encapsulation of devices,[11] and the solar cells based on $MASnI_3$ perovskites have been demonstrated with an efficiency around 6%.[61,62] In addiation, it is worth mentioning that some other tI14 compounds have been synthesized and proposed for solar cells in prior experiments, including MA_2CuX_4[63] and $MA_2PdCl(Br)_4$[46,47]. Our calculations show that these compounds have large m_h^*, and we excluded them according to the $m_h^* \leq 1.5m_0$ criterion. Our calculation results of large m_h^* are also in good agreement with the reduced charge mobility and very low device efficiency observed in the above experimental studies. Notably, Zn and Mg-based

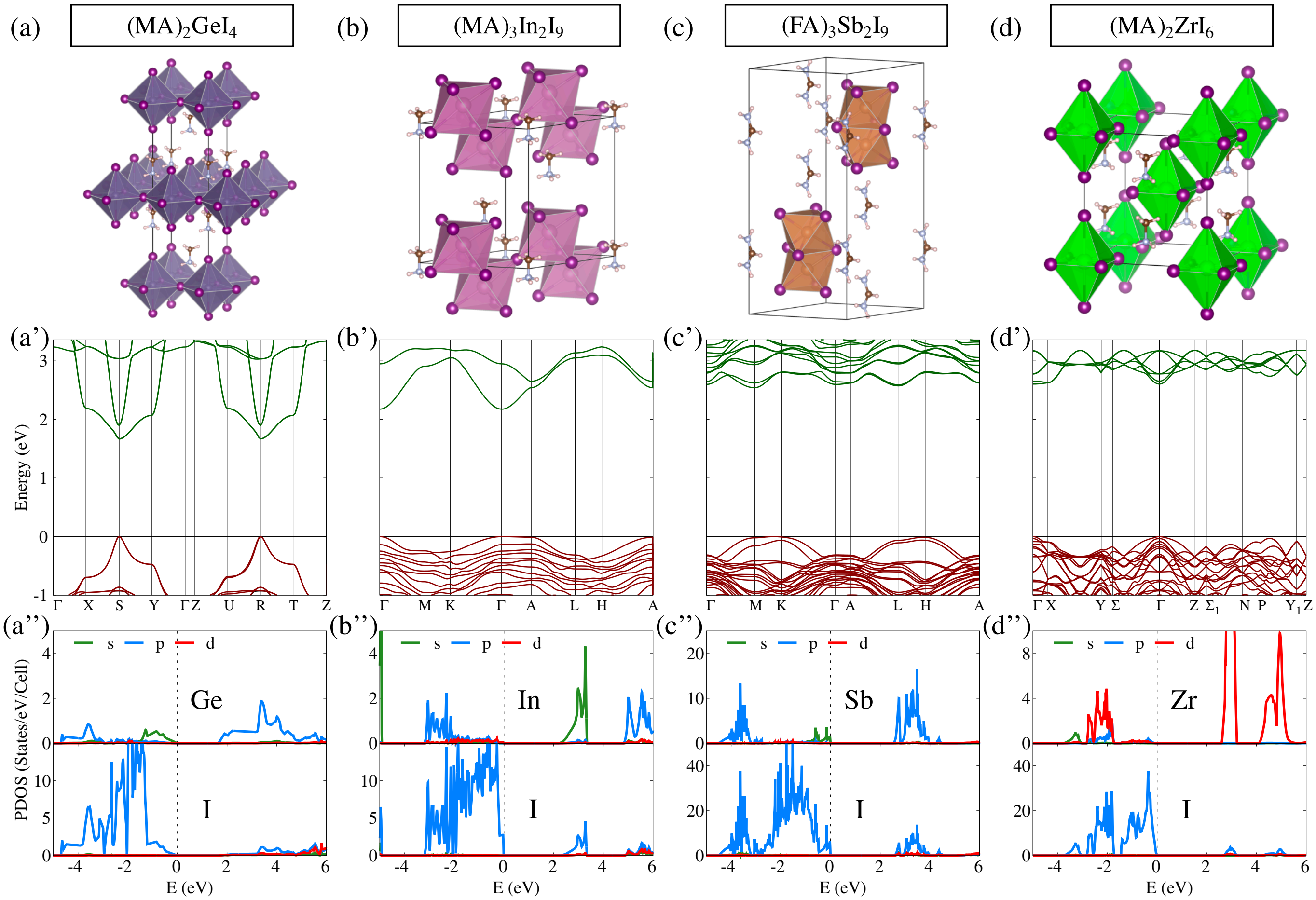

Fig. 3 Representative candidates and their prototype structures: (a) $(MA)_2GeI_4$ in tI14, a tetragonal structure consisting of layers of corner-sharing $B^{II}X_6$ octahedra, (b) $(MA)_3In_2I_9$ in hP14, a hexagonal structure consisting of corrugated layers of corner-sharing $B^{III}X_6$ octahedra, (c) $(FA)_3Sb_2I_9$ in hP28, a hexagonal structure consisting of dimers of face-sharing $B^{III}X_6$ octahedra, and (d) $(MA)_2ZrI_6$ in tI18, a tetragonal structure consisting of isolated $B^{IV}X_6$ octahedra. Their calculated electronic band structures are shown in (a'-d') and atomic orbital projected density of states with HSE06 correction are shown in (a"-d").

tI14 compounds show excellent optoelectronic properties in our calculations, but they were excluded due to large ΔH_f^{diff}.[12]

The B^{3+} candidates take two different crystal structures, hP14 and hP28, both with the formula of $A_3B_2X_9$ (Figure 3b and 3c, respectively). Their difference lies in microscopic structure units. hP14 consists of corner-sharing octahedra in 2D corrugated layers, while hP28 consists of face-sharing octahedra in zero-dimensional (0D) dimers. As competing phases of each other, hP14 and hP28 for the same composition usually have pretty close total energies. To decide which structure stays in the final list, we first followed our criterion for selecting stable competing phases ($\Delta H_f^{diff} \leq 0.015$ eV/atom), and then kept the one with more suitable electronic properties for light-emitter or solar-cell applications. hP14 is usually more favorable due to higher electronic dimensionality[64], but hP28 gives more appropriate properties for some compositions according to our calculations. For example, hP28 $MA_3Sc_2I_9$ yields a direct band gap of proper energy, while hP14 yields an indirect band gap out of the optimal range. In fact, halogen substitution has been demonstrated to lead to phase transition between hP14 and hP28 for $A_3B_2X_9$ compounds[25]. The B^{3+} elements of the selected compounds contain Ga, In, Sb, and Bi. Interestingly, some compounds in hP28 ($Cs_3Bi_2I_9$, $MA_3Bi_2I_9$, and $MA_3Sb_2I_9$) and hP14 ($Cs_3Sb_2I_9$ and $Rb_3Sb_2I_9$) have been fabricated for photovoltaic applications in prior experiments.[24] Accordingly, this class of materials, particularly the new compounds discovered in this work, hold great promise with intrinsic high stability and non-toxicity for the optoelectronic applications.

The B^{4+} candidates adopt two very similar structures, tetragonal tI18 and cubic cF36 (Figure 3d and Figure S1p, respectively). These two structures have the same formula of A_2BX_6 and can convert to each other through phase transition.[65] They both consist of 0D isolated BX_6 octahedra. According to our screening, promising B-site elements in these structures include Zr, Hf, Sn, and Te. Cs_2SnI_6 and Cs_2TeI_6 (cF36) have been incorporated in solar cell devices.[54] These compounds were demonstrated to have high air and moisture stability, proper band gaps, and good electron conductivity. Interestingly, it is noted that Cs_2PdBr_6 (cF36) has also been synthesized and shows promising properties and high stability;[48] its hybrid analogue MA_2PdBr_6 (cF36) was not selected in our list because of a large m_h^* of $1.98m_0$.

4.2 Electronic Structures

In this section, we discuss electronic band structures and atomic orbital projected density of states (PDOS) of representative candidates to reveal electronic properties of all selected compounds. This is because compounds of each prototype structure have common attributes in electronic structures. We selected $(MA)_2GeI_4$, $(MA)_3In_2I_9$, $(FA)_3Sb_2I_9$, and $(MA)_2ZrI_6$ to represent selected compounds of the prototype structures tI14, hP14, hP28, and tI18, respectively. Note that example of cF36 compounds is not shown here because cF36 is very similar to tI18. Figure 3a'-d' and 3a"-d" show the band structures and PDOS of the four representative candidates. The calculated band gap and effective masses data for all final candidates is listed in Table 2 and Table 3.

$(MA)_2GeI_4$, representing the tI14 candidates with B^{2+} cations, shows a direct band gap of 1.66 eV at S point (Figure 3a'). Bands near the conduction band minimum (CBM) and valence band maximum (VBM) are very dispersive, yielding small m_e^* and m_h^* of both $0.11m_0$. Its PDOS shows that conduction band (CB) is mainly contributed by Ge 4*p* orbitals while valence band (VB) is mostly derived from I 5*p* and Ge 4*s* orbitals (Figure 3a").

$(MA)_3In_2I_9$, as an example of the hP14 candidates, shows a direct band gap of 2.18 eV at Γ point (Figure 3b'). Near the band edges, it has a m_e^* of $0.40m_0$, and a m_h^* of $0.61m_0$. Its VB is derived from In 4*d* and I 5*p* orbitals, and the CB is derived from In 5*s* and I 5*p* orbitals (Figure 3b"). $(FA)_3Sb_2I_9$, as an example of hP28 candidates, shows a direct band gap of 2.54 eV at M point (Figure 3c'). The m_e^* and m_h^* were calculated to be $0.39m_0$ and $0.68m_0$, respectively. Its VB consists of Sb 5*s* and I 5*p* orbitals, and the CB consists of Sb 5*p* and I 5*p* orbitals (Figure 3c"). These two candidates both contain B^{3+} cations but adopt different prototype structures. To discuss dependence of electronic structures on crystal structures, we compare the two candidates' valence bands on two parts of the hexagonal *k*-path. On the Γ-A *k*-path, both the hP14 and hP28 candidates show non-dispersive valence bands and large m_h^*. Γ-A corresponds to [001] direction for the hexagonal lattice in real space, and large calculated m_h^* on Γ-A indicates poor hole transport along [001]. This agrees well with poor octahedral connectivity along [001] in the hP14 and hP28 structures (Figure 3b and 3c). On the M-K *k*-path, valence bands of the hP14 candidate is much more dispersive than those of hP28 candidate. This is because M-K corresponds to real-space direction in (001) plane, and the 2D connectivity in hP14 is much more beneficial for hole transport than the 0D connectivity in hP28. Notably, compounds in both of these structures have rather indistinct VBMs, making the band gap types ambiguous. For light-emitting applications, the band gaps become more distinctly direct due to quantum confinement when the compounds are synthesized as nanocrystals.[66,67]

$(MA)_2ZrI_6$, representing the tI18 candidates with B^{4+} cations, shows a distinct direct band gap of 2.60 eV at Γ point, with very dispersive bands near the band edges (Figure 3d'). Its PDOS shows that both VB and CB are mainly contributed by Zr 4*d* and I 5*p* orbitals (Figure 3d"). As mentioned, B^{4+}-based compounds in the tI18 and cF36 structures consist of isolated octahedra, and their B-X bonds are not well connected in a 3D manner. However, the BX_6 octahedra are in close proximity to each other, making it possible for tI18 and cF36 compounds to possess appropriate band gaps and effective masses for the optoelectronic applications[24]. Interestingly, the previously synthesized Cs_2SnI_6 (cF36) shows large m_h^*, which is not suitable for photovoltaics.[54] Our screening results of novel tI18 and cF36 compounds show more suitable properties, especially small and balanced carrier effective masses, and hold great promise for applications in light emitters and solar cells.

5 Conclusion

In summary, we have demonstrated a high-throughput approach to the discovery of hybrid halide compounds beyond perovskites for optoelectronic applications. The discovery process has screened a comprehensive quantum materials repository containing 4507 hybrid compounds using a series of electronic and energetic descriptors including difference of formation enthalpy, decomposition enthalpy, band gap, charge carrier effective masses, and exciton binding energy to select promising candidates for optoelectronic applications. A total number of 23 candidates for light-emitting diodes and 13 candidates for solar energy conversion were selected. These candidates adopt five prototype structures, including tetragonal structure consisting of layers of corner sharing $B^{II}X_6$ (tI14), hexagonal structure consisting of corrugated layers of corner-sharing $B^{III}X_6$ (hP14), hexagonal structure consisting of dimers of face-sharing $B^{III}X_6$ (hP28), tetragonal structure consisting of isolated $B^{IV}X_6$ (tI18), and cubic structure consisiting of isolated $B^{IV}X_6$ (cF36). The tI14 candidates contain B^{II}=Ge, Sn; the hP14 and hP28 candidates contain B^{III}=Ga, In, Sb, Bi; and the tI18 and cF36 candidates contain B^{IV}=Zr, Te, Sn, and Hf. It is important to note that this approach is transformative to the discovery of other types of functional materials.

6 Acknowledgment

This work was supported by the Global Research Outreach (GRO) Program of Samsung Advanced Institute of Technology under the award number 20164974 and National Science Foundation under award number ACI-1550404. This work used the Extreme Science and Engineering Discovery Environment (XSEDE), which is supported by National Science Foundation grant number OCI-1053575, and computational resources supplied by the Department of Defense High Performance Computing Modernization Program (HPCMP).

References

1 A. Kojima, K. Teshima, Y. Shirai, and T. Miyasaka, *Organometal Halide Perovskites as Visible-Light Sensitizers for Photovoltaic Cells*, J. Am. Chem. Soc. **131**, 6050–6051 (2009).

2 S. A. Veldhuis, P. P. Boix, N. Yantara, M. Li, T. C. Sum, N. Mathews, and S. G. Mhaisalkar, *Perovskite Materials for Light-Emitting Diodes and Lasers*, Adv. Mater. **28**, 6804–6834 (2016).

3 S. De Wolf, J. Holovsky, S.-J. Moon, P. Lӧper, B. Niesen, M. Ledinsky, F.-J. Haug, J.-H. Yum, and C. Ballif, *Organometallic Halide Perovskites: Sharp Optical Absorption Edge and Its*

Relation to Photovoltaic Performance, J. Phys. Chem. Lett. **5**, 1035–1039 (2014).

4 C. Wehrenfennig, G. E. Eperon, M. B. Johnston, H. J. Snaith, and L. M. Herz, *High Charge Carrier Mobilities and Lifetimes in Organolead Trihalide Perovskites*, Adv. Mater. **26**, 1584–1589 (2014).

5 A. Walsh, D. O. Scanlon, S. Chen, X. Gong, and S.-H. Wei, *Self-Regulation Mechanism for Charged Point Defects in Hybrid Halide Perovskites*, Angew. Chem. Int. Ed. **54**, 1791–1794 (2015).

6 A. T. Barrows, A. J. Pearson, C. K. Kwak, A. D. Dunbar, A. R. Buckley, and D. G. Lidzey, *Efficient Planar Heterojunction Mixed-Halide Perovskite Solar Cells Deposited via Spray-Deposition*, Energy Environ. Sci. **7**, 2944–2950 (2014).

7 D. Bryant, N. Aristidou, S. Pont, I. Sanchez-Molina, T. Chotchunangatchaval, S. Wheeler, J. R. Durrant, and S. A. Haque, *Light and Oxygen Induced Degradation Limits the Operational Stability of Methylammonium Lead Triiodide Perovskite Solar Cells*, Energy Environ. Sci. **9**, 1655–1660 (2016).

8 B. Conings, J. Drijkoningen, N. Gauquelin, A. Babayigit, J. D'Haen, L. D'Olieslaeger, A. Ethirajan, J. Verbeeck, J. Manca, E. Mosconi, et al., *Intrinsic Thermal Instability of Methylammonium Lead Trihalide Perovskite*, Adv. Energy Mater. **5**, 1500477 (2015).

9 D. Yang, J. Lv, X. Zhao, Q. Xu, Y. Fu, Y. Zhan, A. Zunger, and L. Zhang, *Functionality-Directed Screening of Pb-Free Hybrid Organic–inorganic Perovskites with Desired Intrinsic Photovoltaic Functionalities*, Chem. Mater. **29**, 524–538 (2017).

10 Y. Liao, H. Liu, W. Zhou, D. Yang, Y. Shang, Z. Shi, B. Li, X. Jiang, L. Zhang, L. N. Quan, et al., *Highly Oriented Low-Dimensional Tin Halide Perovskites with Enhanced Stability and Photovoltaic Performance*, J. Am. Chem. Soc. **139**, 6693–6699 (2017).

11 F. Hao, C. C. Stoumpos, P. Guo, N. Zhou, T. J. Marks, R. P. Chang, and M. G. Kanatzidis, *Solvent-Mediated Crystallization of $CH_3NH_3SnI_3$ Films for Heterojunction Depleted Perovskite Solar Cells*, J. Am. Chem. Soc. **137**, 11445–11452 (2015).

12 R. Ali, G.-J. Hou, Z.-G. Zhu, Q.-B. Yan, Q.-R. Zheng, and G. Su, *Predicted Lead-Free Perovskites for Solar Cells*, Chem. Mater. **30**, 718–728 (2018).

13 M. R. Filip, S. Hillman, A. A. Haghighirad, H. J. Snaith, and F. Giustino, *Band Gaps of the Lead-Free Halide Double Perovskites $Cs_2BiAgCl_6$ and $Cs_2BiAgBr_6$ from Theory and Experiment*, J. Phys. Chem. Lett. **7**, 2579–2585 (2016).

14 E. T. McClure, M. R. Ball, W. Windl, and P. M. Woodward, *Cs_2AgBiX_6 (X= Br, Cl): New Visible Light Absorbing, Lead-Free Halide Perovskite Semiconductors*, Chem. Mater. **28**, 1348–1354 (2016).

15 A. H. Slavney, T. Hu, A. M. Lindenberg, and H. I. Karunadasa, *A Bismuth-Halide Double Perovskite with Long Carrier Recombination Lifetime for Photovoltaic Applications*, J. Am. Chem. Soc. **138**, 2138–2141 (2016).

16 F. Wei, Z. Deng, S. Sun, F. Xie, G. Kieslich, D. M. Evans, M. A. Carpenter, P. D. Bristowe, and A. K. Cheetham, *The Synthesis, Structure and Electronic Properties of a Lead-Free Hybrid Inorganic–organic Double Perovskite (MA_2KBiCl_6 (MA= Methylammonium)*, Mater. Horizons **3**, 328–332 (2016).

17 X.-G. Zhao, J.-H. Yang, Y. Fu, D. Yang, Q. Xu, L. Yu, S.-H. Wei, and L. Zhang, *Design of Lead-Free Inorganic Halide Perovskites for Solar Cells via Cation-Transmutation*, J. Am. Chem. Soc. **139**, 2630–2638 (2017).

18 X.-G. Zhao, D. Yang, Y. Sun, T. Li, L. Zhang, L. Yu, and A. Zunger, *Cu–In Halide Perovskite Solar Absorbers*, J. Am. Chem. Soc. **139**, 6718–6725 (2017).

19 T. Nakajima and K. Sawada, *Discovery of Pb-Free Perovskite Solar Cells via High-Throughput Simulation on the K Computer*, J. Phys. Chem. Lett. **8**, 4826–4831 (2017).

20 Z. Xiao, K.-Z. Du, W. Meng, J. Wang, D. B. Mitzi, and Y. Yan, *Intrinsic Instability of $Cs_2In(I)M(III)X_6$ (M= Bi, Sb; X= Halogen) Double Perovskites: A Combined Density Functional Theory and Experimental Study*, J. Am. Chem. Soc. **139**, 6054–6057 (2017).

21 J. Luo, X. Wang, S. Li, J. Liu, Y. Guo, G. Niu, L. Yao, Y. Fu, L. Gao, Q. Dong, et al., *Efficient and Stable Emission of Warm-White Light from Lead-Free Halide Double Perovskites*, Nature **563**, 541 (2018).

22 X.-G. Zhao, D. Yang, J.-C. Ren, Y. Sun, Z. Xiao, and L. Zhang, *Rational Design of Halide Double Perovskites for Optoelectronic Applications*, Joule **2**, 1662–1673 (2018).

23 M.-G. Ju, M. Chen, Y. Zhou, J. Dai, L. Ma, N. P. Padture, and X. C. Zeng, *Toward Eco-Friendly and Stable Perovskite Materials for Photovoltaics*, Joule **2**, 1231–1241 (2018).

24 A. Jodlowski, D. Rodríguez-Padrón, R. Luque, and G. de Miguel, *Alternative Perovskites for Photovoltaics*, Adv. Energy Mater. **8**, 1703120 (2018).

25 F. Jiang, D. Yang, Y. Jiang, T. Liu, X. Zhao, Y. Ming, B. Luo, F. Qin, J. Fan, H. Han, et al., *Chlorine-Incorporation-Induced Formation of the Layered Phase for Antimony-Based Lead-Free Perovskite Solar Cells*, J. Am. Chem. Soc. **140**, 1019–1027 (2018).

26 N. Pai, J. Lu, T. R. Gengenbach, A. Seeber, A. S. Chesman, L. Jiang, D. C. Senevirathna, P. C. Andrews, U. Bach, Y.-B. Cheng, et al., *Silver Bismuth Sulfoiodide Solar Cells: Tuning Optoelectronic Properties by Sulfide Modification for Enhanced Photovoltaic Performance*, Adv. Energy Mater. **9**, 1803396 (2019).

27 S. Curtarolo, W. Setyawan, G. L. W. Hart, M. Jahnatek, R. V. Chepulskii, R. H. Taylor, S. Wang, J. Xue, K. Yang, O. Levy, M. Mehl, H. T. Stokes, D. O. Demchenko, , and D. Morgan, *AFLOW: an Automatic Framework for High-Throughput Materials Discovery*, Comput. Mater. Sci. **58**, 218–226 (2012).

28 G. Kresse and D. Joubert, *From Ultrasoft Pseudopotentials to the Projector Augmented-Wave Method*, Phys. Rev. B **59**, 1758–1775 (1999).

29 J. P. Perdew, K. Burke, and M. Ernzerhof, *Generalized Gradient Approximation Made Simple*, Phys. Rev. Lett. **77**, 3865–3868 (1996).

30 S. Grimme, J. Antony, S. Ehrlich, and H. Krieg, *A Consistent and Accurate Ab Initio Parametrization of Density Functional*

Dispersion Correction (DFT-D) for the 94 Elements H-Pu, J. Chem. Phys. **132**, 154104 (2010).

31 J. Klimeš, D. R. Bowler, and A. Michaelides, *Chemical Accuracy for the van der Waals Density Functional*, J. Phys.: Condens. Matter **22**, 022201 (2009).

32 J. Heyd, G. E. Scuseria, and M. Ernzerhof, *Hybrid Functionals Based on a Screened Coulomb Potential*, Chem. Phys. **118**, 8207–8215 (2003).

33 A. V. Krukau, O. A. Vydrov, A. F. Izmaylov, and G. E. Scuseria, *Influence of the Exchange Screening Parameter on the Performance of Screened Hybrid Functionals*, J. Chem. Phys. **125**, 224106 (2006).

34 S. Curtarolo, W. Setyawan, S. Wang, J. Xue, K. Yang, R. H. Taylor, L. J. Nelson, G. L. W. Hart, S. Sanvito, M. B. Nardelli, N. Mingo, and O. Levy, *AFLOWLIB.ORG: A Distributed Materials Properties Repository from High-Throughput ab Initio Calculations*, Comput. Mater. Sci. **58**, 227–235 (2012).

35 A. Jain, S. P. Ong, G. Hautier, W. Chen, W. D. Richards, S. Dacek, S. Cholia, D. Gunter, D. Skinner, G. Ceder, and K. A. Persson, *Commentary: The Materials Project: A Materials Genome Approach to Accelerating Materials Innovation*, APL Materials **1**, 011002 (2013).

36 C. Zheng and O. Rubel, *Aziridinium Lead Iodide: A Stable, Low-Band-Gap Hybrid Halide Perovskite for Photovoltaics*, J. Phys. Chem. Lett. **9**, 874–880 (2018).

37 L. Wu, P. Lu, Y. Li, Y. Sun, J. Wong, and K. Yang, *First-Principles Characterization of Two-Dimensional* $(CH_3(CH_2)_3NH_3)_2(CH_3NH_3)_{n-1}Ge_nI_{3n+1}$ *Perovskite*, J. Mater. Chem. A **6**, 24389–24396 (2018).

38 J. Even, L. Pedesseau, J.-M. Jancu, and C. Katan, *Importance of Spin–Orbit Coupling in Hybrid Organic/Inorganic Perovskites for Photovoltaic Applications*, J. Phys. Chem. Lett. **4**, 2999–3005 (2013).

39 W. Shockley and H. J. Queisser, *Detailed Balance Limit of Efficiency of P-N Junction Solar Cells*, J. Appl. Phys. **32**, 510–519 (1961).

40 E. F. Schubert, *Light-emitting diodes* (E. Fred Schubert, 2018).

41 J. Nelson, *The physics of solar cells* (World Scientific Publishing Company, 2003).

42 L. Zeng, Y. Yi, C. Hong, J. Liu, N. Feng, X. Duan, L. Kimerling, and B. Alamariu, *Efficiency Enhancement in Si Solar Cells by Textured Photonic Crystal Back Reflector*, Appl. Phys. Lett. **89**, 111111 (2006).

43 S. D. Stranks, G. E. Eperon, G. Grancini, C. Menelaou, M. J. Alcocer, T. Leijtens, L. M. Herz, A. Petrozza, and H. J. Snaith, *Electron-Hole Diffusion Lengths Exceeding 1 Micrometer in an Organometal Trihalide Perovskite Absorber*, Science **342**, 341–344 (2013).

44 X. Y. Chin, D. Cortecchia, J. Yin, A. Bruno, and C. Soci, *Lead Iodide Perovskite Light-Emitting Field-Effect Transistor*, Nat. Commun. **6**, 7383 (2015).

45 S. Siegel and E. Gebert, *The Structures of Hexagonal* $CsCdCl_3$ *and Tetragonal* Cs_2CdCl_4, Acta Cryst. **17**, 790–790 (1964).

46 T. J. Huang, Z. X. Thiang, X. Yin, C. Tang, G. Qi, and H. Gong, $(CH_3NH_3)_2PdCl_4$*: A Compound with Two-Dimensional Organic–Inorganic Layered Perovskite Structure*, Chem. Eur. J. **22**, 2146–2152 (2016).

47 X. Liu, T. J. Huang, L. Zhang, B. Tang, N. Zhang, D. Shi, and H. Gong, *Highly Stable, New, Organic-Inorganic Perovskite* $(CH_3NH_3)_2PdBr_4$*: Synthesis, Structure, and Physical Properties*, Chem. Eur. J. **24**, 4991–4998 (2018).

48 N. Sakai, A. A. Haghighirad, M. R. Filip, P. K. Nayak, S. Nayak, A. Ramadan, Z. Wang, F. Giustino, and H. J. Snaith, *Solution-Processed Cesium Hexabromopalladate (IV),* Cs_2PdBr_6*, for Optoelectronic Applications*, J. Am. Chem. Soc. **139**, 6030–6033 (2017).

49 R. Roccanova, W. Ming, V. R. Whiteside, M. A. McGuire, I. R. Sellers, M.-H. Du, and B. Saparov, *Synthesis, Crystal and Electronic Structures, and Optical Properties of* $(CH_3NH_3)_2CdX_4$ *(X= Cl, Br, I)*, Inorg. Chem. **56**, 13878–13888 (2017).

50 M. A. Green, A. Ho-Baillie, and H. J. Snaith, *The Emergence of Perovskite Solar Cells*, Nat. Photon. **8**, 506–514 (2014).

51 P. Harikesh, H. K. Mulmudi, B. Ghosh, T. W. Goh, Y. T. Teng, K. Thirumal, M. Lockrey, K. Weber, T. M. Koh, S. Li, et al., *Rb as an Alternative Cation for Templating Inorganic Lead-Free Perovskites for Solution Processed Photovoltaics*, Chem. Mater. **28**, 7496–7504 (2016).

52 A. J. Lehner, D. H. Fabini, H. A. Evans, C.-A. Hébert, S. R. Smock, J. Hu, H. Wang, J. W. Zwanziger, M. L. Chabinyc, and R. Seshadri, *Crystal and Electronic Structures of Complex Bismuth Iodides* $A_3Bi_2I_9$ *(A= K, Rb, Cs) Related to Perovskite: Aiding the Rational Design of Photovoltaics*, Chem. Mater. **27**, 7137–7148 (2015).

53 K. M. Boopathi, P. Karuppuswamy, A. Singh, C. Hanmandlu, L. Lin, S. A. Abbas, C. C. Chang, P. C. Wang, G. Li, and C. W. Chu, *Solution-Processable Antimony-Based Light-Absorbing Materials Beyond Lead Halide Perovskites*, J. Mater. Chem. A **5**, 20843–20850 (2017).

54 A. E. Maughan, A. M. Ganose, M. M. Bordelon, E. M. Miller, D. O. Scanlon, and J. R. Neilson, *Defect Tolerance to Intolerance in the Vacancy-Ordered Double Perovskite Semiconductors* Cs_2SnI_6 *and* Cs_2TeI_6, J. Am. Chem. Soc. **138**, 8453–8464 (2016).

55 S. Lu, Q. Zhou, Y. Ouyang, Y. Guo, Q. Li, and J. Wang, *Accelerated Discovery of Stable Lead-Free Hybrid Organic-Inorganic Perovskites via Machine Learning*, Nat. Commun. **9**, 3405 (2018).

56 K. Tanaka, T. Takahashi, T. Ban, T. Kondo, K. Uchida, and N. Miura, *Comparative Study on the Excitons in Lead-Halide-Based Perovskite-Type Crystals* $CH_3NH_3PbBr_3$ $CH_3NH_3PbI_3$, Solid State Commun. **127**, 619–623 (2003).

57 W.-J. Yin, T. Shi, and Y. Yan, *Unusual Defect Physics in* $CH_3NH_3PbI_3$ *Perovskite Solar Cell Absorber*, Appl. Phys. Lett. **104**, 063903 (2014).

58 Z. Xiao, W. Meng, J. Wang, and Y. Yan, *Thermodynamic Stability and Defect Chemistry of Bismuth-Based Lead-Free Double Perovskites*, ChemSusChem **9**, 2628–2633 (2016).

59 T. Li, X. Zhao, D. Yang, M.-H. Du, and L. Zhang, *Intrinsic Defect Properties in Halide Double Perovskites for Optoelectronic*

Applications, Phys. Rev. Appl. **10**, 041001 (2018).

60 K. Kuhar, A. Crovetto, M. Pandey, K. S. Thygesen, B. Seger, P. C. Vesborg, O. Hansen, I. Chorkendorff, and K. W. Jacobsen, *Sulfide Perovskites for Solar Energy Conversion Applications: Computational Screening and Synthesis of the Selected Compound* $LaYS_3$, Energy Environ. Sci. **10**, 2579–2593 (2017).

61 F. Hao, C. C. Stoumpos, D. H. Cao, R. P. Chang, and M. G. Kanatzidis, *Lead-Free Solid-State Organic–Inorganic Halide Perovskite Solar Cells*, Nat. Photon. **8**, 489 (2014).

62 N. K. Noel, S. D. Stranks, A. Abate, C. Wehrenfennig, S. Guarnera, A.-A. Haghighirad, A. Sadhanala, G. E. Eperon, S. K. Pathak, M. B. Johnston, et al., *Lead-Free Organic–Inorganic Tin Halide Perovskites for Photovoltaic Applications*, Energy Environ. Sci. **7**, 3061–3068 (2014).

63 A. M. Elseman, A. E. Shalan, S. Sajid, M. M. Rashad, A. M. Hassan, and M. Li, *Copper-Substituted Lead Perovskite Materials Constructed with Different Halides for Working* $(CH_3NH_3)_2CuX_4$*-Based Perovskite Solar Cells from Experimental and Theoretical View*, ACS Appl. Mater. Interfaces **10**, 11699–11707 (2018).

64 Z. Xiao, W. Meng, J. Wang, D. B. Mitzi, and Y. Yan, *Searching for Promising New Perovskite-Based Photovoltaic Absorbers: the Importance of Electronic Dimensionality*, Mater. Horizons **4**, 206–216 (2017).

65 S. Abrahams, J. Ihringer, and P. Marsh, *Structural and Thermal Dependence of Normal-Mode Condensations in* K_2TeBr_6, Acta Crystallogr. Sect. B **45**, 26–34 (1989).

66 B. Delley and E. Steigmeier, *Quantum Confinement in Si Nanocrystals*, Phys. Rev. B **47**, 1397 (1993).

67 J. K. Ellis, M. J. Lucero, and G. E. Scuseria, *The Indirect to Direct Band Gap Transition in Multilayered* MoS_2 *as Predicted by Screened Hybrid Density Functional Theory*, Appl. Phys. Lett. **99**, 261908 (2011).

Energy & Environmental Science: EE-ART-04-2019-001371.R1

TITLE: High-throughput Computational Design of Organic-inorganic Hybrid Halide Semiconductors Beyond Perovskites for Optoelectronics

Broader context:

Organic-inorganic lead halide perovskites are promising for the next-generation solar cells and light-emitting applications because of their exceptional optoelectronic properties and low-temperature solution processability. However, this class of materials are facing two major challenges including intrinsic poor stability and the presence of toxic lead for their practical applications. To overcome these challenges, great efforts are being devoted to the development of tin-based perovskites and double perovskites, as well as new approaches to protect devices like using encapsulation. In this work, instead of focusing on perovskites, we present a powerful approach to search for novel lead-free hybrid halide semiconductors beyond perovskites from a large variety of prototype structures using high-throughput computations and data-mining techniques. 23 candidates for light-emitting diodes and 13 candidates for solar cells were rapidly identified. All these candidates show appropriate electronic properties and robust stability from ab-initio molecular dynamics simulations. This work demonstrates a new pathway for the large-scale design of novel organic-inorganic optoelectronic materials at a high speed by exploring a large variety of prototype structures. It is important to highlight that this approach is transformative to the discovery of other types of functional materials.